

Article

Cu₂O/CuS/ZnS Nanocomposite Boosts Blue LED-Light-Driven Photocatalytic Hydrogen Evolution

Yu-Cheng Chang , Yung-Chang Chiao and Ya-Xiu Fun

Department of Materials Science and Engineering, Feng Chia University, Taichung 407, Taiwan

* Correspondence: yuchchang@fcu.edu.tw

Abstract: In the present work, we described the synthesis and characterization of the ternary Cu₂O/CuS/ZnS nanocomposite using a facile two-step wet chemical method for blue LED-light-induced photocatalytic hydrogen production. The concentrations of the ZnS precursor and reaction time were essential in controlling the photocatalytic hydrogen production efficiency of the Cu₂O/CuS/ZnS nanocomposite under blue LED light irradiation. The optimized Cu₂O/CuS/ZnS nanocomposite exhibited a maximum photocatalytic hydrogen evolution rate of 1109 $\mu\text{mol h}^{-1} \text{g}^{-1}$, which was remarkably higher than Cu₂O nanostructures. Through the cycle stability it can be observed that the hydrogen production rate of the Cu₂O/CuS/ZnS nanocomposite decreased after 4 cycles (1 cycle = 3 h), but it remained at 82.2% of the initial performance under blue LED light irradiation. These reasons are mainly attributed to the introduction of CuS and ZnS to construct a rationally coupled reaction system, which enables the synergistic utilization of photogenerated carriers and the increased absorption of visible light for boosting blue LED-light-driven photocatalytic hydrogen evolution.

Keywords: Cu₂O/CuS/ZnS nanocomposite; wet chemical; Cu₂O nanostructures; photocatalytic hydrogen production; blue LED light; cycle stability



Citation: Chang, Y.-C.; Chiao, Y.-C.; Fun, Y.-X. Cu₂O/CuS/ZnS Nanocomposite Boosts Blue LED-Light-Driven Photocatalytic Hydrogen Evolution. *Catalysts* **2022**, *12*, 1035. <https://doi.org/10.3390/catal12091035>

Academic Editors: Concetta Ruocco and Marco Martino

Received: 30 August 2022

Accepted: 8 September 2022

Published: 11 September 2022

Publisher's Note: MDPI stays neutral with regard to jurisdictional claims in published maps and institutional affiliations.



Copyright: © 2022 by the authors. Licensee MDPI, Basel, Switzerland. This article is an open access article distributed under the terms and conditions of the Creative Commons Attribution (CC BY) license (<https://creativecommons.org/licenses/by/4.0/>).

1. Introduction

The widespread use of non-renewable energy sources such as coal and oil harms the Earth's environment and causes energy shortages [1,2]. Therefore, people have begun looking for alternative energy sources that are both environmentally friendly and clean, reducing the demand for non-renewable energy sources [3,4]. In today's renewable energy sources, hydrogen is a colorless, odorless, non-toxic, odorless, and combustible gas whose final product is environmentally friendly water [5–7]. Sunlight is the most inexhaustible energy source on earth [8,9]. If sunlight can be used for photocatalytic water splitting to generate hydrogen, it is the best choice for alternative energy [10,11].

When a semiconductor material is excited by a light source larger than its energy gap, electrons can be excited from the valence band (VB) to the conduction band (CB), forming electron–hole pairs [12]. If there is no other transfer method in the process, it is easy to produce reorganization [13,14]. After the photocatalytic decomposition of water to generate hydrogen, the electron–hole pairs were separated and migrated to the photocatalyst surface. Holes oxidize H₂O to H⁺ and O₂, while electrons reduce H⁺ to H₂. When the valence band edge potential is more positive (>+1.23 eV) than the water oxidation potential, and the conduction band edge is more negative (>−0.01) than the water reduction potential, it may be more favorable for photocatalytic water splitting to produce hydrogen [15,16]. However, it is still limited by the problem of electron–hole pair recombination. This result shows that combining different semiconductor materials can improve photocatalytic hydrogen production efficiency [17–19].

Cuprous oxide (Cu₂O) is a p-type semiconductor with an energy gap of 2.17 eV, which has been widely studied and applied due to its low price, non-toxicity, abundant crystal

content, electrocatalytic, and photocatalytic activities [20,21]. Recently, Cu_2O has been widely studied in many applications, such as gas sensors [22,23], supercapacitors [24,25], lithium-ion batteries [26,27], electrocatalysts [28,29], and photocatalysts to reduce carbon dioxide [30]. However, the poor charge separation ability of pure Cu_2O limits its photocatalytic applications [31]. Therefore, coupling Cu_2O with other semiconductor materials is a feasible strategy to improve the separation rate of photogenerated electron–hole pairs [32,33]. So far, different kinds of CuS –semiconductor composites have been synthesized and have significantly improved the photocatalytic efficiency of single materials, such as $\text{Cu}_2\text{O}/\text{TiO}_2$ [31,34], $\text{Cu}_2\text{O}/\text{CuO}$ [35], $\text{Cu}_2\text{O}/\text{ZnO}$ [33], and $\text{Cu}_2\text{O}/\text{g-C}_3\text{N}_4$ [32]. Recently, ternary heterostructures composed of three semiconductors have gained much attention due to their ability to transfer and separate photogenerated electron–hole pairs more efficiently, expand the photoresponse range, and significantly improve photocatalytic performance, such as $\text{Cu}_2\text{O-CO}_3\text{O}_4/\text{CN}$ [36], $\text{MoS}_2\text{-CdS-Cu}_2\text{O}$ [37], $\text{Cu}(\text{OH})_2/\text{Cu}_2\text{O}/\text{C}_3\text{N}_4$ [38], and $\text{ZnO}/\text{Cu}_2\text{O-CuO}$ [39]. However, to our knowledge, no literature has ever reported that the synthesis of the $\text{Cu}_2\text{O}/\text{CuS}/\text{ZnS}$ nanocomposite has been applied in photocatalytic water splitting.

Herein, a ternary $\text{Cu}_2\text{O}/\text{CuS}/\text{ZnS}$ nanocomposite can be synthesized by a facile two-step wet chemical process to validate as a highly efficient water-splitting catalyst under blue LED light irradiation. The improved photocatalytic activities and photostability of the $\text{Cu}_2\text{O}/\text{CuS}/\text{ZnS}$ nanocomposite can be attributed to the highly visible light harvesting and efficient separation of the photogenerated electron–hole pairs prompted by the heterojunction structures.

2. Results and Discussion

X-ray diffraction (XRD) measurements can confirm the crystalline structures of as-prepared photocatalysts. Figure 1a shows the XRD pattern of Cu_2O nanostructures with sharp and strong peaks indicating the high crystallinity of Cu_2O crystals. The diffraction peaks of Cu_2O nanostructures at $2\theta = 29.6^\circ$, 36.4° , 42.3° , 61.4° , 73.6° , and 77.4° can be indexed to cubic phase Cu_2O (JCPDS no. 78-2076), corresponding to the (110), (111), (200), (220), (311), and (222) crystal planes, respectively. In addition, there are two weak diffraction peaks at $2\theta = 35.6^\circ$ and 38.8° , which can be indexed to monoclinic phase CuO (JCPDS no. 80-1268), corresponding to the (-111) and (111) planes, respectively. Figure 1b shows the XRD pattern of the $\text{Cu}_2\text{O}/\text{CuS}/\text{ZnS}$ nanocomposite with small and broad peaks. After the reaction of ZnS precursors, the main as-grown Cu_2O nanostructures were transformed into the hexagonal CuS crystal phase. Only one diffraction peak of Cu_2O nanostructures at $2\theta = 36.4^\circ$ corresponds to the (111) plane of cubic phase Cu_2O (JCPDS no. 78-2076) that was observed. This phenomenon is due to the Kirkendall effect [40]. The formation of the hexagonal CuS crystal phase corresponding to the (102), (103), (107), (108), (200), (202), and (109) planes, respectively, was verified from the diffraction peaks at 29.6° , 32.1° , 48.2° , 53.3° , 56.5° , 57.8° , and 58.6° (JCPDS no. 75-2235). The other two diffraction peaks at $2\theta = 28.5^\circ$ and 33.1° can be indexed to cubic phase ZnS (JCPDS no. 77-2100), corresponding to the (111) and (200) crystal planes, respectively. No additional diffraction peaks are present, suggesting the $\text{Cu}_2\text{O}/\text{CuS}/\text{ZnS}$ nanocomposite is composed of Cu_2O , CuS , and ZnS .

Field-emission scanning electron microscopy (FE-SEM) and field-emission transmission electron microscopy (FE-TEM) can be used to explore the morphological and microstructural features of the as-prepared photocatalysts. Figure 2a shows the top-view FE-SEM image of Cu_2O nanostructures grown via the wet chemical method under the low reaction temperature of 50°C for 1 h. Cu_2O nanostructures revealed a more scattered size and shape. The FE-TEM image (Figure 2b) further confirms the microstructures of Cu_2O nanostructures showing apparent aggregation, which is consistent with the FE-SEM image. The selected area electron diffraction (SAED) pattern (Figure 2c) of Cu_2O nanostructures exhibited polycrystalline diffraction rings. The concentric rings (from inside to outside) can, respectively, be indexed to the cubic phase Cu_2O (JCPDS no. 78-2076) and monoclinic phase CuO (JCPDS no. 80-1268) [41]. This result is also consistent with the above XRD

result. In the high-resolution TEM (HRTEM) image (Figure 2d), the lattice fringes of 0.301, 0.246, and 0.252 nm match with the (110) and (111) planes of cubic phase Cu_2O (JCPDS no. 78-2076) and the (-111) plane of monoclinic phase CuO (JCPDS no. 80-1268), respectively, which agrees with the above result of Figure 2c.

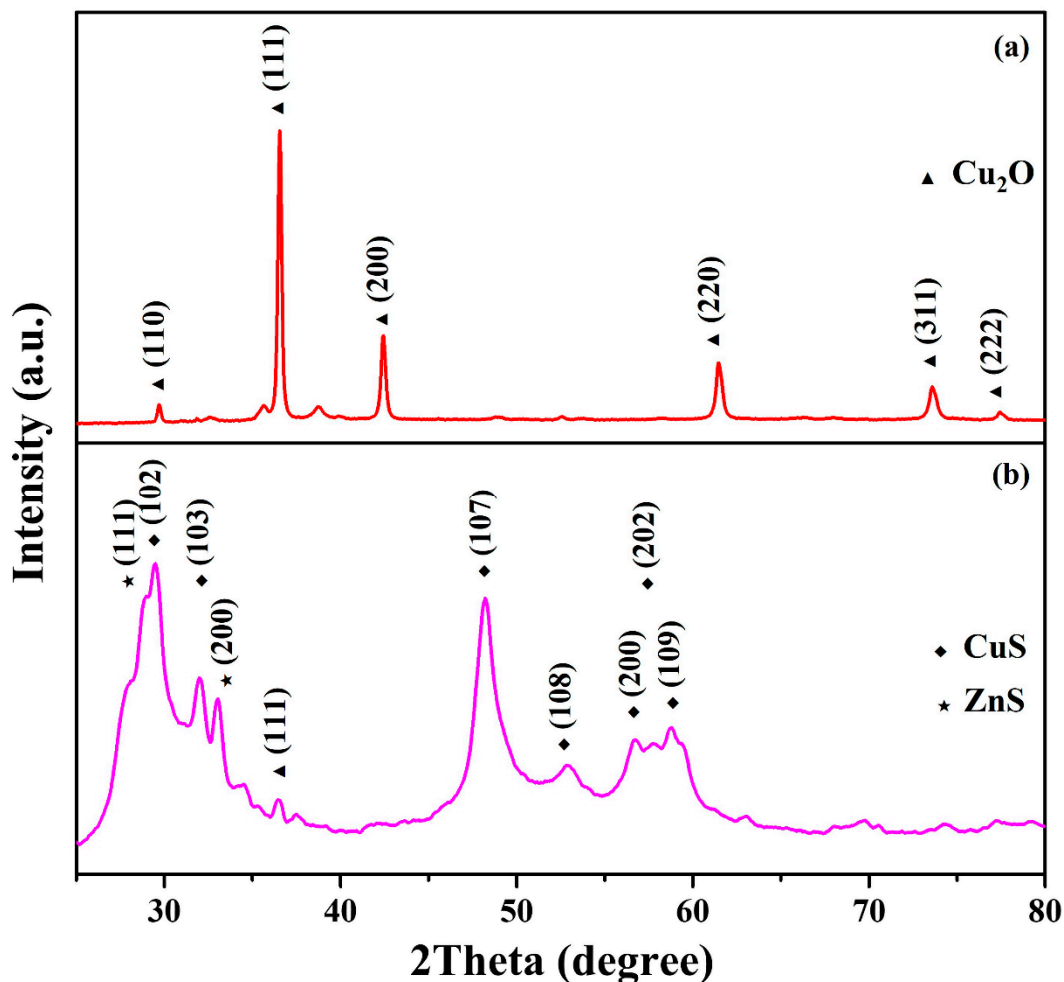


Figure 1. The XRD spectra of (a) Cu_2O nanostructures and (b) the $\text{Cu}_2\text{O}/\text{CuS}/\text{ZnS}$ nanocomposite grown at the 10 mM ZnS precursor and 20 min reaction time.

Figure 3a shows the top-view FE-SEM image of $\text{Cu}_2\text{O}/\text{CuS}/\text{ZnS}$ nanocomposite with 0.02 g Cu_2O nanostructures and 10 mM ZnS precursor grown via the wet chemical method at $100\text{ }^\circ\text{C}$ for 1 h. Compared with Cu_2O nanostructures, $\text{Cu}_2\text{O}/\text{CuS}/\text{ZnS}$ nanocomposite tends to be smaller and more uniform in size. Furthermore, the FE-TEM image (Figure 3b) further confirms the microstructures of the $\text{Cu}_2\text{O}/\text{CuS}/\text{ZnS}$ nanocomposite, showing an evident aggregation phenomenon between particles, which is consistent with the FE-SEM image. The SAED pattern (Figure 3b inset) of the $\text{Cu}_2\text{O}/\text{CuS}/\text{ZnS}$ nanocomposite also revealed polycrystalline diffraction rings. The concentric rings (from inside to outside) can, respectively, be indexed to the cubic phase ZnS (JCPDS no. 77-2100), hexagonal phase CuS (JCPDS no. 75-2235), and cubic phase Cu_2O (JCPDS no. 78-2076). Three lattice spacing measurements of 0.319, 0.313, and 0.246 nm can be detected from the HRTEM image in Figure 3c, which corresponds to the (101), (111), and (111) diffraction planes of hexagonal phase CuS, cubic phase ZnS, and cubic phase Cu_2O , respectively. The EDS elemental mapping images (Figure 3d) further confirmed that Cu, O, Zn, and S were present and evenly distributed throughout the $\text{Cu}_2\text{O}/\text{CuS}/\text{ZnS}$ nanocomposite.

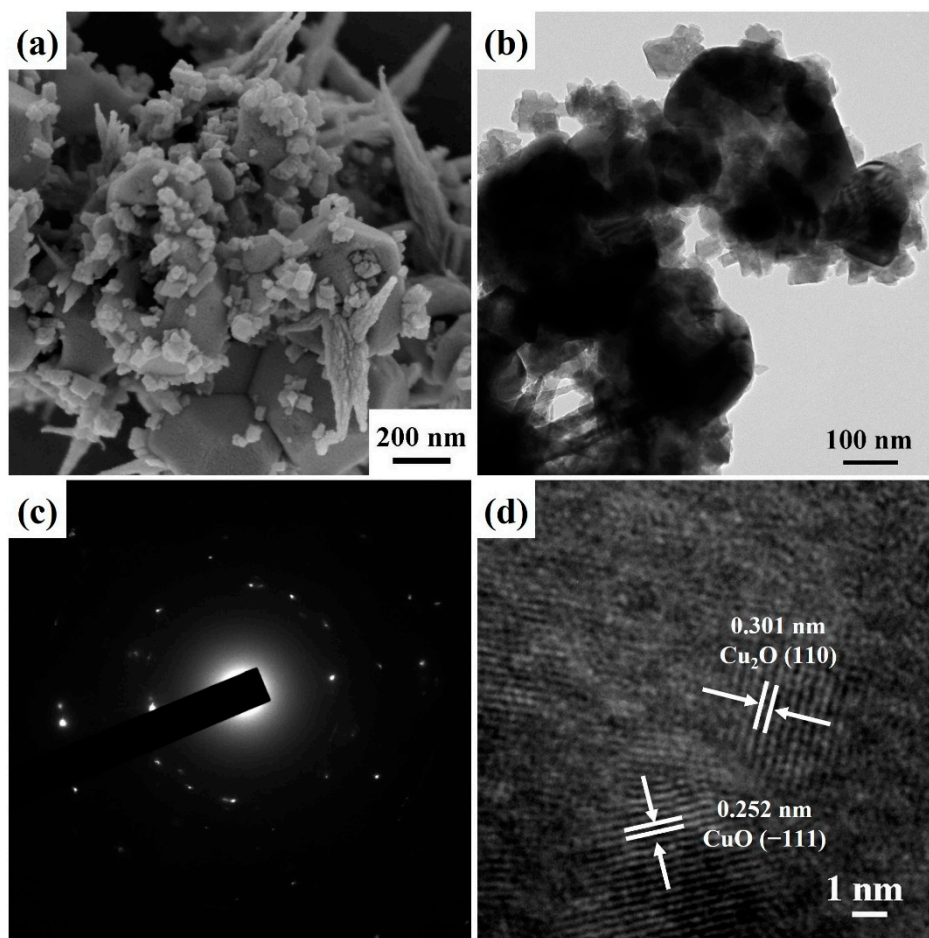


Figure 2. (a) FE-SEM, (b) FE-TEM, (c) SAED pattern, and (d) HRTEM images of Cu_2O nanostructures.

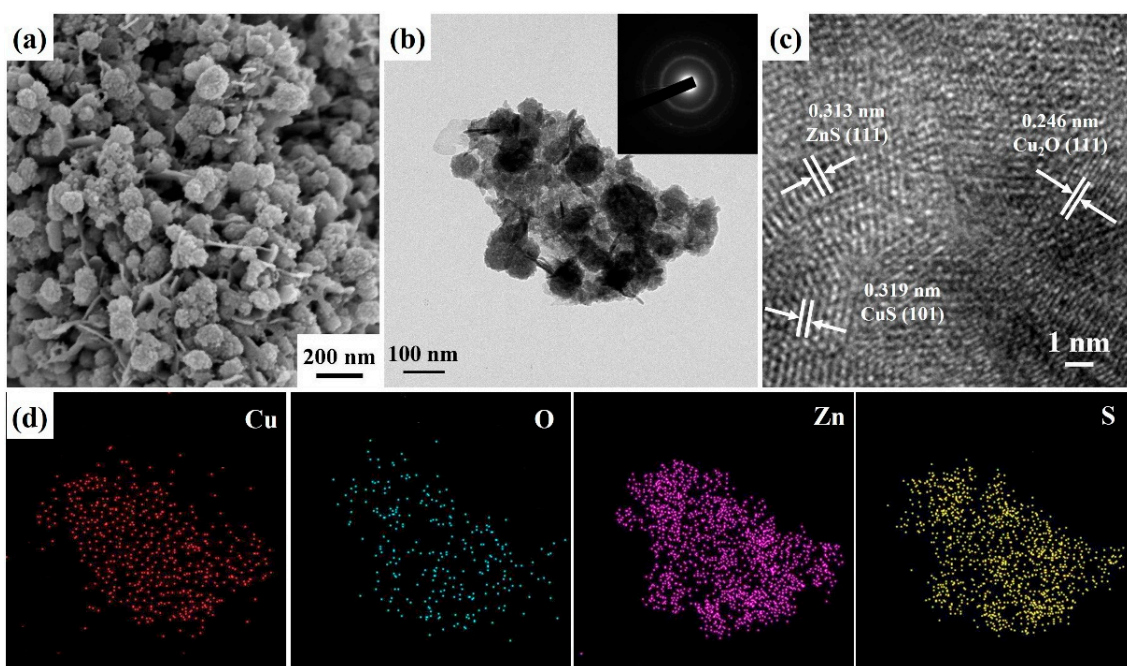


Figure 3. (a) FE-SEM, (b) FE-TEM and SAED pattern (inset), (c) HRTEM, and (d) EDS mapping images of the $\text{Cu}_2\text{O}/\text{CuS}/\text{ZnS}$ nanocomposite grown at the 10 mM ZnS precursor and 20 min reaction time.

X-ray photoelectron spectroscopy (XPS) analysis can be used to verify the surface composition and bonding of the Cu₂O/CuS/ZnS nanocomposite, as shown in Figure 4. The survey XPS spectrum (Figure 4a) demonstrates that Cu₂O/CuS/ZnS nanocomposite includes Cu, O, Zn, and S elements. The presence of C 1s can be attributed to the pump oil in the vacuum system of the XPS device or to the organic layer coated on the Cu₂O/CuS/ZnS nanocomposite [14]. The high-resolution Cu 2p_{3/2} spectrum (Figure 4b) shows that two peaks at 931.7 eV and 932.6 eV correspond to the different oxidation states of Cu⁺ and Cu²⁺ ions for Cu₂O and CuS, respectively. In addition, the high-resolution Cu 2p_{1/2} spectrum (Figure 4c) also reveals that two peaks at 951.7 eV and 953.2 eV correspond to the different oxidation states of Cu⁺ and Cu²⁺ ions for Cu₂O and CuS, respectively [42,43]. According to the O 1s spectrum (Figure 4d), there are three peaks at 530.4 eV, 531.5 eV, and 532.4 eV, which are attributed to Cu–O–Cu (lattice O, O_L), oxygen vacancies or defect (O_V), and chemisorbed or dissociated (O_C), respectively [17,44]. The peaks of Figure 4e at 1021.8 and 1044.9 eV belong to Zn 2p_{3/2} and Zn 2p_{1/2}, respectively, suggesting the presence of ZnS [45,46]. According to the S 2p spectrum (Figure 4f), the peaks at 161.5 and 162.6 eV can be assigned to S 2p_{3/2} and S 2p_{1/2}, which indicates that S exists as S²⁻ [47]. These results confirm that the Cu₂O/CuS/ZnS nanocomposite was successfully constructed.

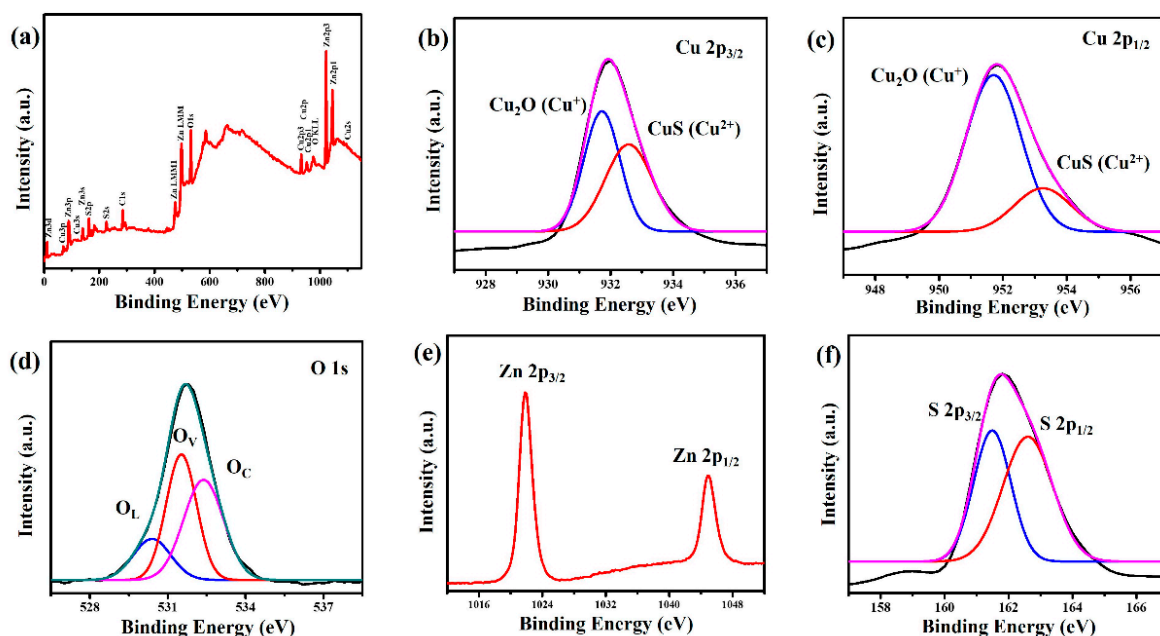


Figure 4. The XPS spectra of the Cu₂O/CuS/ZnS nanocomposite: (a) survey spectrum, (b) Cu 2p_{3/2}, (c) Cu 2p_{1/2}, (d) O 1s, (e) Zn 2p, and (f) S 2p.

In order to evaluate the photocatalytic performance of the Cu₂O/CuS/ZnS nanocomposite, blue LED-light-driven hydrogen production via water splitting was accomplished using sodium sulfide as a sacrificial reagent. Figure 5a shows the comparable photocatalytic hydrogen production activities of the Cu₂O/CuS/ZnS nanocomposite grown at different concentrations of ZnS precursors (such as 2.5, 5, 10, and 20 mM). The as-synthesized photocatalysts' average hydrogen evolution rates (HER) are 0 (Cu₂O nanostructures), 6.433 (2.5 mM ZnS precursor), 120.9 (5 mM ZnS precursor), 601.2 (10 mM ZnS precursor), and 388.6 (20 mM ZnS precursor) $\mu\text{mol h}^{-1} \text{g}^{-1}$. No hydrogen can be detected in the Cu₂O nanostructures. Cu₂O nanostructures exhibited inferior hydrogen production activities, attributed to the fast recombination of photogenerated electron–hole pairs [31,33]. The HER of Cu₂O/CuS/ZnS nanocomposites gradually increased with ZnS precursor concentration. The HER of the Cu₂O/CuS/ZnS nanocomposite decreased significantly with a ZnS precursor concentration greater than 10 mM. This phenomenon is also consistent with the previous literature [48]. Figure 5b compares the photocatalytic hydrogen production

efficiency of the $\text{Cu}_2\text{O}/\text{CuS}/\text{ZnS}$ nanocomposite grown at different reaction times. The average HERs of the $\text{Cu}_2\text{O}/\text{CuS}/\text{ZnS}$ nanocomposite are 473.0 (10 min), 1109 (20 min), 870.8 (30 min), and 716.5 (40 min) $\mu\text{molh}^{-1}\text{g}^{-1}$. The HER of the $\text{Cu}_2\text{O}/\text{CuS}/\text{ZnS}$ nanocomposite gradually increased with the reaction time from 10 to 20 min. However, the further increase resulted in a decreased HER of the $\text{Cu}_2\text{O}/\text{CuS}/\text{ZnS}$ nanocomposite. This result may be attributed to the fact that too long a reaction time may lead to the complete reaction of Cu_2O to form CuS , which in turn reduces the efficiency of light absorption and electron and hole transfer, thereby inhibiting the efficiency of photocatalytic hydrogen production.

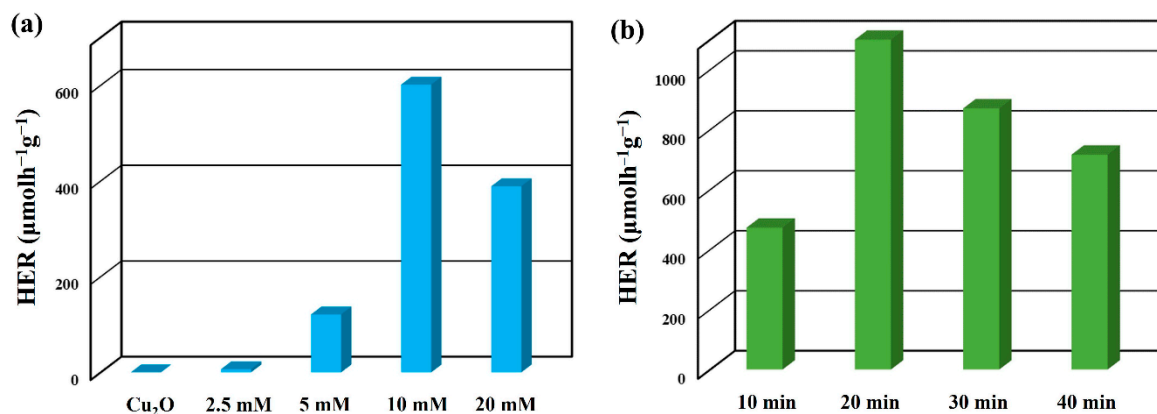


Figure 5. The average HER of the $\text{Cu}_2\text{O}/\text{CuS}/\text{ZnS}$ nanocomposite grown at different (a) ZnS precursor concentrations and (b) reaction times under blue LED light irradiation.

The optical absorption properties of the Cu_2O nanostructures and $\text{Cu}_2\text{O}/\text{CuS}/\text{ZnS}$ nanocomposite were evaluated by UV–Vis DRS spectroscopy, as shown in Figure 6a. Compared with Cu_2O nanostructures, the $\text{Cu}_2\text{O}/\text{CuS}/\text{ZnS}$ nanocomposite exhibited stronger absorption bands in the visible region. This result reveals that the decoration of CuS and ZnS can significantly increase the visible light absorption (475–800 nm) of the $\text{Cu}_2\text{O}/\text{CuS}/\text{ZnS}$ nanocomposite, thereby improving its photocatalytic hydrogen production. PL emission peaks on semiconductor materials mainly originate from photoinduced electron/hole pair recombination [49]. Cu_2O nanostructures exhibit a stronger green emission peak at 532 nm (2.33 eV), which is attributed to the electron–hole pair recombination of the near-bandgap emission (NBE) of Cu_2O [50,51]. When Cu_2O is combined with CuS and ZnS , the photoinduced carriers can migrate between the composite materials, thereby inhibiting the photoinduced electron–hole pair recombination. This result is beneficial in enhancing the photocatalytic hydrogen production efficiency of the $\text{Cu}_2\text{O}/\text{CuS}/\text{ZnS}$ nanocomposite.

Figure 6c shows the possible photocatalytic hydrogen production mechanism of the $\text{Cu}_2\text{O}/\text{CuS}/\text{ZnS}$ nanocomposite for photocatalytic hydrogen production by the above analysis results. Ion exchange resin coats the materials Cu_2O , CuS , and ZnS in indium tin oxide (ITO) glass and then measures the flat band potential by cyclic voltammogram [52,53]. The VB and CB of Cu_2O , CuS , and ZnS are consistent with the previous reports [54,55]. The Cu_2O , CuS , and ZnS CB positions are -1.4 eV, -0.5 eV, and -0.99 eV, respectively. The Cu_2O , CuS , and ZnS VB positions are 0.93 eV, 1.91 eV, and 2.52 eV, respectively. Intrinsic defects can generate new electric state bands at the bottom of the CB of ZnS , combined with narrowing the band gap to enhance visible light absorption. The photogenerated electrons of Cu_2O , CuS , and ZnS can be excited from their VB to CB under visible light irradiation. The photogenerated electrons in the CB of ZnS and Cu_2O can be transferred to the CB of CuS . CuS can act as an electron sink to capture and reduce hydrogen ions to hydrogen. Meanwhile, the photogenerated holes in the VB of ZnS can be transferred to the CuS or Cu_2O to oxidize water to oxygen or hydrogen ions. Therefore, this photocatalytic process can improve the separation of photogenerated charge carriers and facilitate their photocatalytic hydrogen production.

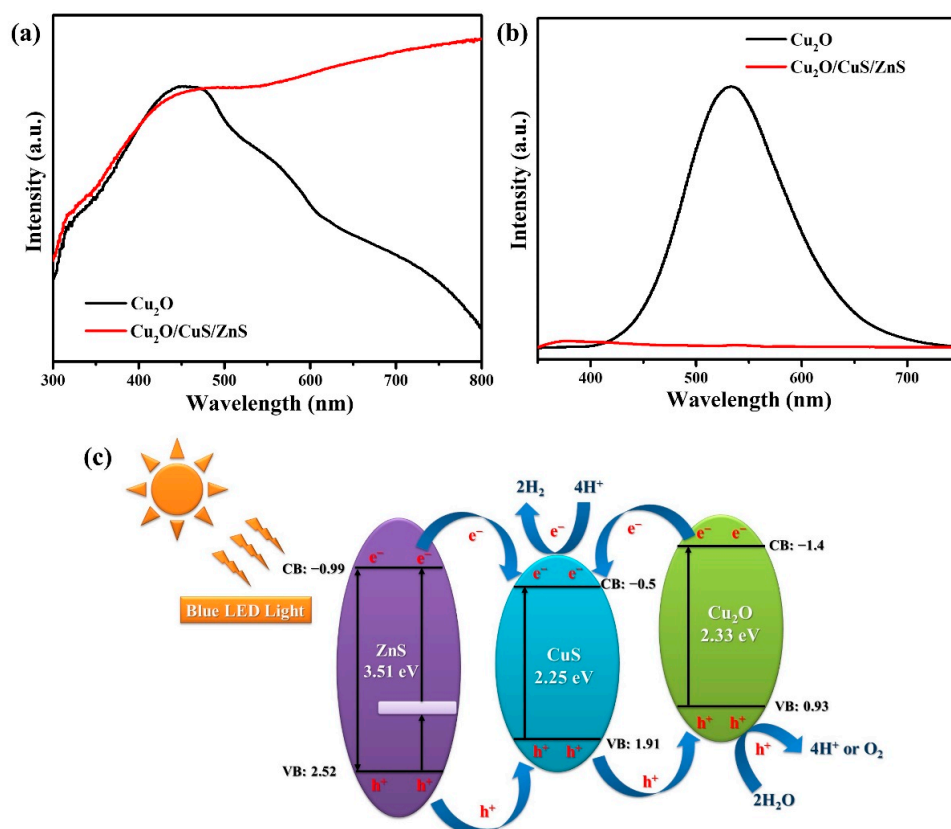


Figure 6. The (a) UV–Vis absorption and (b) PL spectra of Cu_2O nanostructures and the $\text{Cu}_2\text{O}/\text{CuS}/\text{ZnS}$ nanocomposite. (c) Schematic diagram of the electron transfer mechanism of the $\text{Cu}_2\text{O}/\text{CuS}/\text{ZnS}$ nanocomposite under blue LED light irradiation.

Sacrificial reagents are often used for the photocatalytic splitting of water to generate hydrogen to enhance the performance of oxidation reactions in aqueous media because pure water oxidation is usually inefficient [56]. Figure 7a displays the effects of four sacrificial agents (such as folic acid, methanol, sodium sulfate, and sodium sulfide) on the photocatalytic efficiency of the optimized $\text{Cu}_2\text{O}/\text{CuS}/\text{ZnS}$ nanocomposite (10 mM ZnS precursor and 20 min reaction time) without adjusted pH value. All sacrificial agents were formulated at the same 0.1 M concentration. The order of average HER with the $\text{Cu}_2\text{O}/\text{CuS}/\text{ZnS}$ nanocomposite is sodium sulfide ($622.7 \mu\text{mol h}^{-1}\text{g}^{-1}$) > folic acid ($4.753 \mu\text{mol h}^{-1}\text{g}^{-1}$) > sodium sulfate ($0 \mu\text{mol h}^{-1}\text{g}^{-1}$) = methanol ($0 \mu\text{mol h}^{-1}\text{g}^{-1}$). There are two main reasons for using sodium sulfide as a sacrificial reagent for the best hydrogen production efficiency. First, sulfide ions (S^{2-} , dissociated sodium sulfide) can be adsorbed on the photocatalyst and react with photogenerated holes, thereby inhibiting the recombination of electron and hole pairs. Second, sulfide ions can reduce the photocorrosion rate of metal sulfide semiconductors by combining with metal ions and inhibiting sulfide defects, thereby improving the stability of photocatalytic hydrogen production [57,58].

The optimum pH value of photocatalytic hydrogen production mainly depends on the properties of the sacrificial agent and the adsorption on the surface of the photocatalyst [59]. The different pH values can be adjusted from their initial value by adding dropwise 1M HCl. Figure 7b displays the effects of pH values on the photocatalytic efficiency of the optimized $\text{Cu}_2\text{O}/\text{CuS}/\text{ZnS}$ nanocomposite (10 mM ZnS precursor and 20 min reaction time). The average HERs of the $\text{Cu}_2\text{O}/\text{CuS}/\text{ZnS}$ nanocomposite are 0 (pH = 3), 336.2 (pH = 6), 473.5 (pH = 9), 1109 (pH = 12), and $622.8 \mu\text{mol h}^{-1}\text{g}^{-1}$ (pH = 12.8, without adjusted), respectively. From pH 3 to 12, the photocatalytic hydrogen production efficiency revealed significant improvement with the gradual increase in pH value. This phenomenon can be mainly attributed to the dissociation of HS^- and S^{2-} , which increases gradually

with increased pH value [60]. When the concentration of hydroxide ions is too high, many photogenerated hydrogen ions can further react with hydroxide ions to form water, thereby reducing the photocatalytic hydrogen production efficiency [61]. This result indicates that the $\text{Cu}_2\text{O}/\text{CuS}/\text{ZnS}$ nanocomposite exhibits the best photocatalytic hydrogen production efficiency at $\text{pH} = 12$.

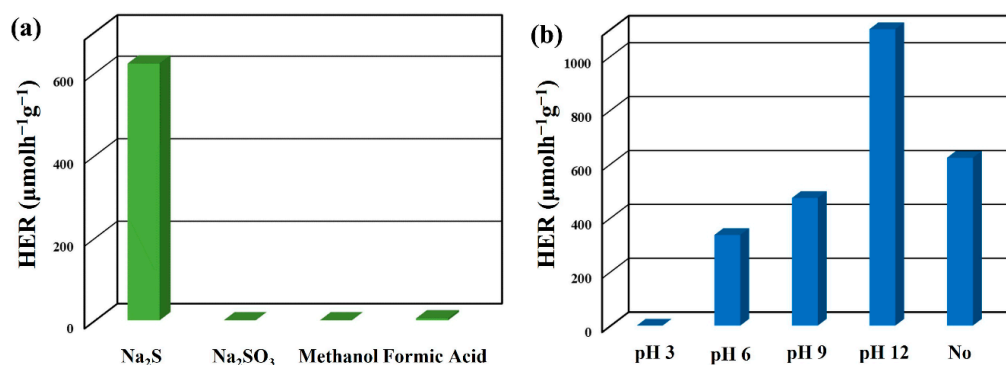


Figure 7. The average HER of optimized $\text{Cu}_2\text{O}/\text{CuS}/\text{ZnS}$ nanocomposite at (a) sacrificial reagents and (b) different pH values.

The practicality of photocatalysts mainly depends on their stability and reusability [62]. Therefore, it was used consecutively to evaluate the photocatalyst's stability to ensure its recyclability in photocatalytic experiments. In addition, the light source is the main factor due to the overall photocatalytic efficiency depending on the irradiation intensity [63]. Herein, the reusability of the optimized $\text{Cu}_2\text{O}/\text{CuS}/\text{ZnS}$ nanocomposite is also evaluated by performing the water-splitting reaction for 3 h with four cycles under blue LED light (Figure 8a) and white LED light (Figure 8b) irradiation. As a result, the average HERs of optimized the $\text{Cu}_2\text{O}/\text{CuS}/\text{ZnS}$ nanocomposite are 1025, 1029, 911.2, and 851.6 $\mu\text{molh}^{-1}\text{g}^{-1}$, respectively, under blue LED light irradiation. On the other hand, the average HERs of the optimized $\text{Cu}_2\text{O}/\text{CuS}/\text{ZnS}$ nanocomposite are 647.8, 493.8, 483.9, and 407.4 $\mu\text{molh}^{-1}\text{g}^{-1}$, respectively, under white LED light irradiation. After the reusability tests, the photocatalytic hydrogen production efficiency of the $\text{Cu}_2\text{O}/\text{CuS}/\text{ZnS}$ nanocomposite revealed a slight decrease ($\sim 17.8\%$ and $\sim 37.1\%$) under the blue LED light and white LED light irradiation, respectively. This result shows that the $\text{Cu}_2\text{O}/\text{CuS}/\text{ZnS}$ nanocomposite exhibited the best photocatalytic hydrogen generation efficiency and recycle stability under blue LED light irradiation. The possible reason is that the energy of the white LED light is dispersed in two prominent bands, but blue light only has a single band. Therefore, this band's energy can be concentrated, increasing the photocatalytic hydrogen production efficiency.

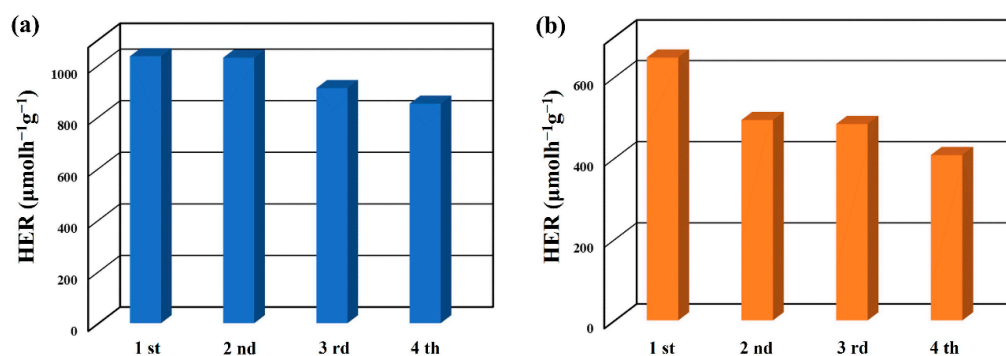


Figure 8. The cycling stability of the optimized $\text{Cu}_2\text{O}/\text{CuS}/\text{ZnS}$ nanocomposite under (a) blue LED light and (b) white LED light irradiation.

3. Material and Methods

3.1. Preparation of Cu₂O Nanostructures

Cu₂O nanostructures were synthesized by a simple wet chemical method. In a typical procedure, 2.5 mL 0.1 M CuCl₂·2H₂O, 0.9 mL 0.1 M NaOH, 12 mL 0.1 M NH₂OH·HCl, and 0.435 g SDS were dispersed in 34.6 mL deionized water. The mixture was heated at 50 °C under vigorous stirring for 1 h. After cooling, the as-prepared products were collected, washed with deionized water, and dried at 70 °C for 2 h.

3.2. Preparation of the Cu₂O/CuS/ZnS Nanocomposite

The Cu₂O/CuS/ZnS nanocomposite was synthesized using a simple wet chemical method. In a typical procedure, different concentrations of ZnS precursor (equimolar zinc nitrate hexahydrate and thioacetamide) were dissolved in 100 mL of deionized water. The 0.02 g Cu₂O nanostructures were dispersed in a 100 mL reaction solution with different concentrations of ZnS precursor. The mixture was heated at 100 °C under vigorous stirring for 1 h. After cooling, the as-prepared products were collected, washed with deionized water, and dried at 70 °C for 2 h.

3.3. Characterization

The phase structure, morphology, microstructure, and optical properties of as-synthesized photocatalysts were, respectively, measured by X-ray powder diffraction (Bruker D2 phaser system, USA), field-emission scanning electron microscopy (FESEM, Hitachi S-4800, Japan), field-emission transmission electron microscopy (FETEM, JEOL-2100F, Japan), X-ray photoelectron spectroscopy (XPS, ULVAC-PHI PHI 5000 Versaprobe II system, Japan), photoluminescence (PL, 325 nm He-Cd laser, Taiwan), and UV-Vis DRS spectroscopy (U-2900, Hitachi, Japan).

3.4. Photocatalytic Activity Measurement

A photocatalytic reactor (PCX50B Discover, Perfect Light, China) with blue LED light sources (5W, λ_{max} = 420 nm) or white LED light (5W, two λ_{max} at 450 nm and 550 nm) was used to evaluate photocatalytic hydrogen production. In a typical experiment, as-prepared photocatalysts (20 mg) were dispersed into a mixed solution with 0.1 M sacrificial reagents (such as sodium sulfide, sodium sulfite, methanol, and ethanol) and 50 mL of deionized water (≥18.3 MΩ·cm). After a degassing pretreatment, the experimental device was carried out for 30 min to remove air. Then, the hydrogen amounts were measured using gas chromatography (GC, Shimadzu GC-2014) with a thermal conductivity detector (TCD).

4. Conclusions

A facile two-step wet chemical process synthesizes a new noble metal-free heterostructure of Cu₂O/CuS/ZnS nanocomposite for blue LED-light-induced photocatalytic hydrogen production. The optimized Cu₂O/CuS/ZnS nanocomposite could achieve H₂ evolution rates of up to 1109 μmolh⁻¹g⁻¹ at a pH value = 12 and 0.1 M sodium sulfide under blue LED light irradiation. This result can be attributed to the formation of CuS and ZnS on Cu₂O nanostructures, which can effectively absorb visible light emission and promote the separation efficiency of photogenerated electron-hole pairs under blue LED light irradiation. Furthermore, reusability experiments prove that the Cu₂O/CuS/ZnS nanocomposite exhibits excellent stability for a long-term photocatalytic process under blue LED light irradiation.

Author Contributions: Funding acquisition, methodology, project administration, resources, software, supervision, validation, writing—original draft, and writing—review and editing, Y.-C.C. (Yu-Cheng Chang); formal analysis, investigation, and data curation, Y.-C.C. (Yung-Chang Chiao) and Y.-X.F. All authors have read and agreed to the published version of the manuscript.

Funding: This research was funded by the Ministry of Science and Technology of Taiwan (MOST 109-2221-E-035-041-MY3).

Data Availability Statement: Not applicable.

Acknowledgments: The authors appreciate the Precision Instrument Support Center of Feng Chia University for providing the fabrication and measurement facilities.

Conflicts of Interest: The authors declare no conflict of interest.

References

1. Dincer, I. Renewable energy and sustainable development: A crucial review. *Renew. Sustain. Energy Rev.* **2000**, *4*, 157–175. [[CrossRef](#)]
2. Gielen, D.; Boshell, F.; Saygin, D.; Bazilian, M.D.; Wagner, N.; Gorini, R. The role of renewable energy in the global energy transformation. *Energy Strategy Rev.* **2019**, *24*, 38–50. [[CrossRef](#)]
3. Ellabban, O.; Abu-Rub, H.; Blaabjerg, F. Renewable energy resources: Current status, future prospects and their enabling technology. *Renew. Sustain. Energy Rev.* **2014**, *39*, 748–764. [[CrossRef](#)]
4. Kuang, Y.; Zhang, Y.; Zhou, B.; Li, C.; Cao, Y.; Li, L.; Zeng, L. A review of renewable energy utilization in islands. *Renew. Sustain. Energy Rev.* **2016**, *59*, 504–513. [[CrossRef](#)]
5. Filippov, S.P.; Yaroslavtsev, A.B. Hydrogen energy: Development prospects and materials. *Russ. Chem. Rev.* **2021**, *90*, 627–643. [[CrossRef](#)]
6. Yue, M.; Lambert, H.; Pahon, E.; Roche, R.; Jemei, S.; Hissel, D. Hydrogen energy systems: A critical review of technologies, applications, trends and challenges. *Renew. Sustain. Energy Rev.* **2021**, *146*, 111180. [[CrossRef](#)]
7. Martin, A.; Agnoletti, M.-F.; Brangier, E. Users in the design of Hydrogen Energy Systems: A systematic review. *Int. J. Hydrog. Energy* **2020**, *45*, 11889–11900. [[CrossRef](#)]
8. Kannan, N.; Vakeesan, D. Solar energy for future world: A review. *Renew. Sustain. Energy Rev.* **2016**, *62*, 1092–1105. [[CrossRef](#)]
9. Kumar, V.; Shrivastava, R.L.; Untawale, S.P. Solar Energy: Review of Potential Green & Clean Energy for Coastal and Offshore Applications. *Aquat. Procedia* **2015**, *4*, 473–480. [[CrossRef](#)]
10. Fajrina, N.; Tahir, M. A critical review in strategies to improve photocatalytic water splitting towards hydrogen production. *Int. J. Hydrog. Energy* **2019**, *44*, 540–577. [[CrossRef](#)]
11. Acar, C.; Dincer, I.; Naterer, G.F. Review of photocatalytic water-splitting methods for sustainable hydrogen production. *Int. J. Energy Res.* **2016**, *40*, 1449–1473. [[CrossRef](#)]
12. Chou, C.-M.; Chang, T.-T.; Chen, C.-Y.; Chang, Y.-C. Constructing Er-Doped ZnO/CuS/Au Core-Shell Nanowires with Enhanced Photocatalytic and SERS Properties. *Catalysts* **2021**, *11*, 1347. [[CrossRef](#)]
13. Kitano, M.; Hara, M. Heterogeneous photocatalytic cleavage of water. *J. Mater. Chem.* **2010**, *20*, 627–641. [[CrossRef](#)]
14. Chang, Y.-C.; Lin, Y.-W.; Lu, M.-Y. Construction of MoS₂/ZnO heterostructures as highly efficient photocatalysts for enhanced visible-light decomposition of methylene blue and hydrogen evolution. *Mater. Chem. Phys.* **2021**, *266*, 124560. [[CrossRef](#)]
15. Ran, J.; Zhang, J.; Yu, J.; Jaroniec, M.; Qiao, S.Z. Earth-abundant cocatalysts for semiconductor-based photocatalytic water splitting. *Chem. Soc. Rev.* **2014**, *43*, 7787–7812. [[CrossRef](#)]
16. Ismael, M. A review and recent advances in solar-to-hydrogen energy conversion based on photocatalytic water splitting over doped-TiO₂ nanoparticles. *Sol. Energy* **2020**, *211*, 522–546. [[CrossRef](#)]
17. Chang, Y.-C.; Tasi, C.-L.; Ko, F.-H. Construction of ZnIn₂S₄/ZnO heterostructures with enhanced photocatalytic decomposition and hydrogen evolution under blue LED irradiation. *Int. J. Hydrog. Energy* **2021**, *46*, 10281–10292. [[CrossRef](#)]
18. Chang, Y.-C.; Syu, S.-Y.; Wu, Z.-Y. Fabrication of ZnO-In₂S₃ composite nanofiber as highly efficient hydrogen evolution photocatalyst. *Mater. Lett.* **2021**, *302*, 130435. [[CrossRef](#)]
19. Li, K.; Zhang, Y.; Lin, Y.-Z.; Wang, K.; Liu, F.-T. Versatile Functional Porous Cobalt–Nickel Phosphide–Carbon Cocatalyst Derived from a Metal–Organic Framework for Boosting the Photocatalytic Activity of Graphitic Carbon Nitride. *ACS Appl. Mater. Interfaces* **2019**, *11*, 28918–28927. [[CrossRef](#)]
20. Wu, T.; Zheng, H.; Kou, Y.; Jin, S.; Jiang, Y.; Gao, M.; Chen, L.; Kadasala, N.R.; Liu, Y. Rhombic dodecahedral Cu₂O/Ag-3D Fe₃O₄ micro-flower composites for water purification under visible light irradiation. *J. Alloy. Compd.* **2021**, *858*, 157698. [[CrossRef](#)]
21. Zhou, T.; Zang, Z.; Wei, J.; Zheng, J.; Hao, J.; Ling, F.; Tang, X.; Fang, L.; Zhou, M. Efficient charge carrier separation and excellent visible light photoresponse in Cu₂O nanowires. *Nano Energy* **2018**, *50*, 118–125. [[CrossRef](#)]
22. Wang, N.; Tao, W.; Gong, X.; Zhao, L.; Wang, T.; Zhao, L.; Liu, F.; Liu, X.; Sun, P.; Lu, G. Highly sensitive and selective NO₂ gas sensor fabricated from Cu₂O–CuO microflowers. *Sens. Actuators B Chem.* **2022**, *362*, 131803. [[CrossRef](#)]
23. Wang, N.; Zhou, Y.; Chen, K.; Wang, T.; Sun, P.; Wang, C.; Chuai, X.; Zhang, S.; Liu, X.; Lu, G. Double shell Cu₂O hollow microspheres as sensing material for high performance n-propanol sensor. *Sens. Actuators B Chem.* **2021**, *333*, 129540. [[CrossRef](#)]
24. Liu, P.; Qin, K.; Wen, S.; Wang, L.; He, F.; Liu, E.; He, C.; Shi, C.; Li, J.; Li, Q.; et al. In situ fabrication of Ni(OH)₂/Cu₂O nanosheets on nanoporous NiCu alloy for high performance supercapacitor. *Electrochim. Acta* **2018**, *283*, 970–978. [[CrossRef](#)]
25. Purushothaman, S.; Jeyasubramanian, K.; Muthuselvi, M.; Hikku, G.S. Cu₂O nanosheets decorated CuMnO₂ nanosphere electrode deposited on Cu foil as high-performance supercapacitor electrode. *Mater. Sci. Semicond. Processing* **2021**, *121*, 105366. [[CrossRef](#)]
26. Kim, E.-S.; Kim, M.-C.; Moon, S.-H.; Shin, Y.-K.; Lee, J.-E.; Choi, S.; Park, K.-W. Surface modified and size-controlled octahedral Cu₂O nanostructured electrodes for lithium-ion batteries. *J. Alloy. Compd.* **2019**, *794*, 84–93. [[CrossRef](#)]

27. Zhang, L.; Li, Q.; Xue, H.; Pang, H. Fabrication of Cu₂O-based Materials for Lithium-Ion Batteries. *ChemSusChem* **2018**, *11*, 1581–1599. [[CrossRef](#)]
28. Roy, A.; Jadhav, H.S.; Gil Seo, J. Cu₂O/CuO Electrocatalyst for Electrochemical Reduction of Carbon Dioxide to Methanol. *Electroanalysis* **2021**, *33*, 705–712. [[CrossRef](#)]
29. Xu, H.; Feng, J.-X.; Tong, Y.-X.; Li, G.-R. Cu₂O–Cu Hybrid Foams as High-Performance Electrocatalysts for Oxygen Evolution Reaction in Alkaline Media. *ACS Catal.* **2017**, *7*, 986–991. [[CrossRef](#)]
30. Mohan, S.; Honnappa, B.; Augustin, A.; Shanmugam, M.; Chuaicham, C.; Sasaki, K.; Ramasamy, B.; Sekar, K. A Critical Study of Cu₂O: Synthesis and Its Application in CO₂ Reduction by Photochemical and Electrochemical Approaches. *Catalysts* **2022**, *12*, 445. [[CrossRef](#)]
31. Zhang, Y.-H.; Liu, M.-M.; Chen, J.-L.; Xie, K.-F.; Fang, S.-M. Dendritic branching Z-scheme Cu₂O/TiO₂ heterostructure photocatalysts for boosting H₂ production. *J. Phys. Chem. Solids* **2021**, *152*, 109948. [[CrossRef](#)]
32. Ng, B.-J.; Tang, J.-Y.; Ow, L.Y.; Kong, X.Y.; Ng, Y.H.; Putri, L.K.; Chai, S.-P. Nanoscale p-n junction integration via the synergetic hybridization of facet-controlled Cu₂O and defect modulated g-C₃N_{4-x} atomic layers for enhanced photocatalytic water splitting. *Mater. Today Energy* **2022**, 101102. [[CrossRef](#)]
33. Park, B.H.; Park, H.; Kim, T.; Yoon, S.J.; Kim, Y.; Son, N.; Kang, M. S-scheme assisted Cu₂O/ZnO flower-shaped heterojunction catalyst for breakthrough hydrogen evolution by water splitting. *Int. J. Hydrog. Energy* **2021**, *46*, 38319–38335. [[CrossRef](#)]
34. Muscetta, M.; Andreozzi, R.; Clarizia, L.; Di Somma, I.; Marotta, R. Hydrogen production through photoreforming processes over Cu₂O/TiO₂ composite materials: A mini-review. *Int. J. Hydrog. Energy* **2020**, *45*, 28531–28552. [[CrossRef](#)]
35. Seo, Y.J.; Arunachalam, M.; Ahn, K.-S.; Kang, S.H. Integrating heteromixed Cu₂O/CuO photocathode interface through a hydrogen treatment for photoelectrochemical hydrogen evolution reaction. *Appl. Surf. Sci.* **2021**, *551*, 149375. [[CrossRef](#)]
36. Shaikh, Z.A.; Moiseev, N.; Mikhaylov, A.; Yüksel, S. Facile Synthesis of Copper Oxide–Cobalt Oxide/Nitrogen-Doped Carbon (Cu₂O–Co₃O₄/CN) Composite for Efficient Water Splitting. *Appl. Sci.* **2021**, *11*, 9974. [[CrossRef](#)]
37. Kumar, U.; Das Chakraborty, S.; Sahu, R.K.; Bhattacharya, P.; Mishra, T. Improved Interfacial Charge Transfer on Noble Metal-Free Biomimetic CdS-Based Tertiary Heterostructure @ 2D MoS₂-CdS-Cu₂O with Enhanced Photocatalytic Water Splitting. *Adv. Mater. Interfaces* **2022**, *9*, 2101680. [[CrossRef](#)]
38. Mahzoon, S.; Haghghi, M.; Nowee, M.; Zeinalzadeh, H. Sonoprecipitation design of novel efficient all-solid Z-Scheme Cu(OH)₂/Cu₂O/C₃N₄ nanophotocatalyst applied in water splitting for H₂ production: Synergetic effect of Cu-Based cocatalyst (Cu(OH)₂) and electron mediator (Cu). *Sol. Energy Mater. Sol. Cells* **2021**, *219*, 110772. [[CrossRef](#)]
39. Yoo, H.; Kahng, S.; Hyeun Kim, J. Z-scheme assisted ZnO/Cu₂O-CuO photocatalysts to increase photoactive electrons in hydrogen evolution by water splitting. *Sol. Energy Mater. Sol. Cells* **2020**, *204*, 110211. [[CrossRef](#)]
40. Cai, L.; Sun, Y.; Li, W.; Zhang, W.; Liu, X.; Ding, D.; Xu, N. CuS hierarchical hollow microcubes with improved visible-light photocatalytic performance. *RSC Adv.* **2015**, *5*, 98136–98143. [[CrossRef](#)]
41. Zhang, Z.; Song, R.; Yu, Z.; Huang, W. Crystal-plane effect of Cu₂O templates on compositions, structures and catalytic performance of Ag/Cu₂O nanocomposites. *CrystEngComm* **2019**, *21*, 2002–2008. [[CrossRef](#)]
42. Ji, Q.; Yan, X.; Xu, J.; Wang, C.; Wang, L. Fabrication of hollow type-II and Z-scheme In₂O₃/TiO₂/Cu₂O photocatalyst based on In-MIL-68 for efficient catalytic degradation of tetracycline. *Sep. Purif. Technol.* **2021**, *265*, 118487. [[CrossRef](#)]
43. Giribabu, K.; Oh, S.Y.; Suresh, R.; Kumar, S.P.; Manigandan, R.; Munusamy, S.; Gnanamoorthy, G.; Kim, J.Y.; Huh, Y.S.; Narayanan, V. Sensing of picric acid with a glassy carbon electrode modified with CuS nanoparticles deposited on nitrogen-doped reduced graphene oxide. *Microchim. Acta* **2016**, *183*, 2421–2430. [[CrossRef](#)]
44. Rosen, J.; Hutchings, G.S.; Jiao, F. Ordered Mesoporous Cobalt Oxide as Highly Efficient Oxygen Evolution Catalyst. *J. Am. Chem. Soc.* **2013**, *135*, 4516–4521. [[CrossRef](#)] [[PubMed](#)]
45. Liang, Y.-C.; Wang, C.-C. Surface crystal feature-dependent photoactivity of ZnO–ZnS composite rods via hydrothermal sulfidation. *RSC Adv.* **2018**, *8*, 5063–5070. [[CrossRef](#)] [[PubMed](#)]
46. Mao, M.; Jiang, L.; Wu, L.; Zhang, M.; Wang, T. The structure control of ZnS/graphene composites and their excellent properties for lithium-ion batteries. *J. Mater. Chem. A* **2015**, *3*, 13384–13389. [[CrossRef](#)]
47. Adhikari, S.; Sarkar, D.; Madras, G. Hierarchical Design of CuS Architectures for Visible Light Photocatalysis of 4-Chlorophenol. *ACS Omega* **2017**, *2*, 4009–4021. [[CrossRef](#)]
48. Huang, J.; Shi, Z.; Dong, X. Nickel sulfide modified TiO₂ nanotubes with highly efficient photocatalytic H₂ evolution activity. *J. Energy Chem.* **2016**, *25*, 136–140. [[CrossRef](#)]
49. Chang, Y.-C.; Hsu, C.-C. Synergetic effect of carbon black as co-catalyst for enhanced visible-light photocatalytic activity and stability on ZnO nanoparticles. *Solid State Sci.* **2020**, *107*, 106366. [[CrossRef](#)]
50. Liu, X.; Xu, M.; Zhang, X.; Wang, W.; Feng, X.; Song, A. Pulsed-laser-deposited, single-crystalline Cu₂O films with low resistivity achieved through manipulating the oxygen pressure. *Appl. Surf. Sci.* **2018**, *435*, 305–311. [[CrossRef](#)]
51. Sekar, K.; Chuaicham, C.; Vellaichamy, B.; Li, W.; Zhuang, W.; Lu, X.; Ohtani, B.; Sasaki, K. Cubic Cu₂O nanoparticles decorated on TiO₂ nanofiber heterostructure as an excellent synergistic photocatalyst for H₂ production and sulfamethoxazole degradation. *Appl. Catal. B Environ.* **2021**, *294*, 120221. [[CrossRef](#)]
52. Ge, H.; Tian, H.; Zhou, Y.; Wu, S.; Liu, D.; Fu, X.; Song, X.-M.; Shi, X.; Wang, X.; Li, N. Influence of Surface States on the Evaluation of the Flat Band Potential of TiO₂. *ACS Appl. Mater. Interfaces* **2014**, *6*, 2401–2406. [[CrossRef](#)] [[PubMed](#)]

53. Bhattacharya, C.; Lee, H.C.; Bard, A.J. Rapid Screening by Scanning Electrochemical Microscopy (SECM) of Dopants for Bi₂WO₆ Improved Photocatalytic Water Oxidation with Zn Doping. *J. Phys. Chem. C* **2013**, *117*, 9633–9640. [[CrossRef](#)]
54. Gu, Y.; Xu, Z.; Guo, L.; Wan, Y. ZnO nanoplate-induced phase transformation synthesis of the composite ZnS/In(OH)₃/In₂S₃ with enhanced visible-light photodegradation activity of pollutants. *CrystEngComm* **2014**, *16*, 10997–11006. [[CrossRef](#)]
55. Huang, J.-Y.; Hsieh, P.-L.; Naresh, G.; Tsai, H.-Y.; Huang, M.H. Photocatalytic Activity Suppression of CdS Nanoparticle-Decorated Cu₂O Octahedra and Rhombic Dodecahedra. *J. Phys. Chem. C* **2018**, *122*, 12944–12950. [[CrossRef](#)]
56. Burek, B.O.; Timm, J.; Bahnemann, D.W.; Bloh, J.Z. Kinetic effects and oxidation pathways of sacrificial electron donors on the example of the photocatalytic reduction of molecular oxygen to hydrogen peroxide over illuminated titanium dioxide. *Catal. Today* **2019**, *335*, 354–364. [[CrossRef](#)]
57. Schneider, J.; Bahnemann, D.W. Undesired Role of Sacrificial Reagents in Photocatalysis. *J. Phys. Chem. Lett.* **2013**, *4*, 3479–3483. [[CrossRef](#)]
58. Bao, N.; Shen, L.; Takata, T.; Domen, K. Self-Templated Synthesis of Nanoporous CdS Nanostructures for Highly Efficient Photocatalytic Hydrogen Production under Visible Light. *Chem. Mater.* **2008**, *20*, 110–117. [[CrossRef](#)]
59. Mills, A.; Le Hunte, S. An overview of semiconductor photocatalysis. *J. Photochem. Photobiol. A Chem.* **1997**, *108*, 1–35. [[CrossRef](#)]
60. Preethi, V.; Kanmani, S. Photocatalytic hydrogen production using Fe₂O₃-based core shell nano particles with ZnS and CdS. *Int. J. Hydrog. Energy* **2014**, *39*, 1613–1622. [[CrossRef](#)]
61. Strataki, N.; Antoniadou, M.; Dracopoulos, V.; Lianos, P. Visible-light photocatalytic hydrogen production from ethanol–water mixtures using a Pt–CdS–TiO₂ photocatalyst. *Catal. Today* **2010**, *151*, 53–57. [[CrossRef](#)]
62. Khan, A.U.; Arooj, A.; Tahir, K.; Ibrahim, M.M.; Jevtovic, V.; Al-Abdulkarim, H.A.; Saleh, E.A.M.; Al-Shehri, H.S.; Amin, M.A.; Li, B. Facile fabrication of novel Ag₂S-ZnO/GO nanocomposite with its enhanced photocatalytic and biological applications. *J. Mol. Struct.* **2022**, *1251*, 131991. [[CrossRef](#)]
63. Park, Y.-K.; Kim, B.-J.; Jeong, S.; Jeon, K.-J.; Chung, K.-H.; Jung, S.-C. Characteristics of hydrogen production by photocatalytic water splitting using liquid phase plasma over Ag-doped TiO₂ photocatalysts. *Environ. Res.* **2020**, *188*, 109630. [[CrossRef](#)] [[PubMed](#)]